High Critical Current Density and Enhanced Pinning in Superconducting Films of $YBa_2Cu_3O_{7-\delta}$ Nanocomposites with Embedded $BaZrO_3$, $BaHfO_3$, $BaTiO_3$ and $SrZrO_3$ Nanocrystals

Javier Díez-Sierra[1], Pedro López-Domínguez[1], Hannes Rijckaert[1], Mark Rikel[2], Jens Hänisch[3], Mukarram Zaman Khan[4], Martina Falter[2], Jan Bennewitz[5], Hannu Huhtinen[4], Sebastian Schäfer[6], Robert Müller[6], Stephan Andreas Schunk[6], Petriina Paturi[4], Michael Bäcker[2], Klaartje De Buysser[1], Isabel Van Driessche[1,*].

[1] Ghent University, Dept. of Chemistry, Krijgslaan 281 - S3, 9000 Ghent, Belgium
[2] Deutsche Nanoschicht GmbH, Heisenbergstr. 16, 53359 Rheinbach, Germany
[3] Karlsruhe Institute of Tech., ITEP, Hermann-von-Helmholtz-Pl. 1, 76131 Eggenstein-Leopoldshafen, Germany
[4] University of Turku, Wihuri Physical Laboratory, Dept. of Physics and Astronomy, 20014 Turku, Finland
[5] BASF SE, Advanced Materials & Systems Research, Carl-Bosch-Str. 38, 67056 Ludwigshafen, Germany
[6] hte GmbH, Kurpfalzring 104, 69123 Heidelberg, Germany
* Corresponding author: Isabel.VanDriessche@UGent.be

Abstract

Chemical solution deposition (CSD) of $YBa_2Cu_3O_{7-\delta}$ (YBCO) nanocomposites from colloidal precursor solutions containing double metal oxide preformed nanocrystals is a promising, cost-effective and reproducible approach to produce superconducting films with high critical current density (J_c) and enhanced pinning. Here, the influence of the preformed nanocrystal composition on the microstructure and superconducting properties of the YBCO nanocomposite films is studied, with a focus on establishing a simple and scalable process to grow nanocomposites that can be transferred to grow nano-added coated conductors. Colloidal stable $BaZrO_3$, $BaHfO_3$, $BaTiO_3$ and $SrZrO_3$ nanocrystals (3-6 nm in diameter) were synthesized and added to an environment-friendly low-fluorine YBCO precursor solution. High-quality superconducting layers were grown on $LaAlO_3$ single-crystal substrates from these four nanocomposite precursor solutions in a single deposition process, without the need of a seed layer, yielding J_c of 4-5 MA/cm² at 77 K in self-field. The different YBCO microstructures produced by the four types of nanocrystals and the resulting microstrain of the films are compared and related with the magnetic-field and angular dependence of J_c. We demonstrate the $BaHfO_3$-containing nanocomposite as the best-performing with a homogeneous distribution of nanoparticles with 7 nm in average diameter and a high density of stacking faults, which leads to some of the best superconducting properties ever achieved via low-fluorine CSD. The J_c exhibits a much smoother decay in applied magnetic fields and a much more isotropic behaviour for non-parallel magnetic fields, and the pinning force is increased by a factor of 3.5 at 77 K and 1 T with respect to the pristine film.

Keywords

Nanocomposite, Nanoparticles, superconducting, YBCO, thin film, vortex pinning, chemical solution deposition, perovskite

Introduction

$YBa_2Cu_3O_{7-\delta}$ (YBCO) coated conductors have an extraordinary electrical performance and power density ideal for more efficient and compact cables, power transformers, motors and generators.[1-2] However, factors such as the high cost, the low availability, and the reduction of critical current density (J_c) in the presence of moderate to high magnetic fields have prevented the expansion of coated conductors in the power market.[1-3] Chemical solution deposition (CSD) has the potential to fulfill the demand of high-quality epitaxial YBCO films with excellent performance and high throughput, while the addition of preformed nanocrystals can reduce the J_c decay with magnetic field.[4-7] CSD offers the potential to fabricate coated conductors with high deposition rates at moderate precursor and investment cost. However, when coated conductors operate in high magnetic fields, their performance is strongly reduced due to vortex motion.[1-3] The incorporation of artificial pinning centres in the form of nanoscale secondary phases has been proven to enhance vortex pinning increasing the in-field J_c as well as the J_c isotropy with respect to the direction of the magnetic field.[7-10] In this respect, two approaches are possible: the *in situ* and the *ex situ* formation of artificial pinning centres. In the *in situ* approach, extra metal-organic salts are added to the YBCO precursor solution which form secondary phases during the YBCO growth by spontaneous segregation. This *in situ* method is well investigated and has shown important pinning enhancement; however, it has reproducibility issues providing little control over the segregation of nanoparticles and their size and spatial distribution.[11-14] In contrast, the *ex situ* approach utilizes colloidal stable nanocrystals that are synthesized in advance and then added to the YBCO precursor solution.

This offers superior control over size, shape, crystallinity and concentration of the nanocrystals and therefore over the final microstructure of the nanocomposite films.[15-19] However, previous studies have shown that improper choice of nanoparticle composition leads to agglomeration of the preformed nanoparticles during the thermal processing of the layers[18-19] as well as to accumulation of the nanocrystals on the substrate[15] or at the YBCO surface[17]. These effects worsen the superconducting properties and hinder the pinning enhancement. The composition of the preformed nanocrystals is, thus, an important factor to control the homogeneity and the size of the final nanocrystals in the crystallized layer. Metal oxide nanocrystals such as ZrO_2, CeO_2 and HfO_2 react with Ba^{2+} during YBCO growth to form $BaZrO_3$, $BaCeO_3$ and $BaHfO_3$, respectively, which leads to coarsening of the nanoparticles.[16-17, 20] To avoid this, double metal oxide nanocrystals are introduced which are more chemically inert and should not react with Ba^{2+}. Only very recently the first nanocomposites with preformed double metal oxide nanocrystals have been reported.[21-22] Nanocomposites with $BaZrO_3$ and $BaHfO_3$ nanocrystals were obtained by Obradors *et al*.[21] and Li *et al*.[22] with self-field J_c of 3.0-4.5 MA/cm^2 at 77 K and enhanced pinning efficiency. However, the high fluorine content of the all-trifluoroacetate (TFA) YBCO precursor solutions used and the need of a 25-50 nm pristine YBCO layer (so-called seed layer) to improve YBCO texture and to prevent the accumulation of nanocrystals at the film-substrate interface[15] complicates the up-scaling to a continuous industrial reel-to-reel process with high throughput. Moreover, the best pinning properties are obtained via a tuned thermal treatment with a heating rate of 1200 ºC/min which is extremely difficult to reproduce on industrial scale.

The aim of this work is to study the effect of the preformed nanocrystal composition on the final YBCO microstructure and pinning properties of the nanocomposites. This work will also focus on establishing a simple scalable process to grow nanocomposites, that can be used to manufacture nanocrystal-added coated conductors, eliminating every step which cannot be

replicated at an industrial scale. In this respect, low-fluorine YBCO precursor solutions (with ~69% reduction in F content) based on propionates instead of TFA are used. The industrial production of CSD-based YBCO films is progressing towards the use of more environment-friendly precursors with lower fluorine content to reduce the release of toxic fluorinated compounds during the thermal process.[7, 23-24] This implies another challenge for the *ex situ* approach because the colloidal nanocrystal solutions stable in TFA-based precursor solutions (pH = 2) might not be stable in the higher pH of the low-fluorine solution (pH = 6).[19] Moreover, the choice of ligand has been proven to have a dramatic effect on the final properties of the nanocomposite[16, 25]. In this work 2-[2-(2-methoxyethoxy)ethoxy]acetic acid[26-27] is used since it can stabilize all the as-synthesized double metal oxide nanocrystals—$BaZrO_3$ (BZO), $BaHfO_3$ (BHO), $BaTiO_3$ (BTO), and $SrZrO_3$ (SZO)—and is completely decomposed after the pyrolysis at 400 °C of the films (see Supporting Information (SI), Figure S1), leaving no organic residues in the layers. The four types of nanocrystals (3-6 nm in diameter) are synthesized via a microwave heating method that allows much faster and more reproducible production of nanocrystals than the conventional solvothermal method and is easier to scale up[15, 28]. After synthesis, the nanocrystals are purified and stabilized in polar solvent (*e.g.* methanol) forming monodisperse colloidal suspensions without agglomerations that can directly be added to the low-fluorine YBCO precursor solution. The resulting colloidal YBCO solutions are then deposited on $LaAlO_3$ (LAO) single-crystal substrates in a single deposition step without seed layer and are crystallized following the same thermal treatment used for pristine YBCO, ensuring the feasibility of the industrial scale-up. High-quality superconducting layers are obtained from the pristine and the four colloidal YBCO precursor solutions yielding self-field J_c of 4-5 MA/cm² at 77 K. The different defect landscapes and the resulting microstrain of the YBCO matrix in the four nanocomposites and the pristine film are compared, and their effects on the magnetic-field and angular dependence of J_c are studied. Among the studied

combinations, the BHO nanocomposite exhibits the properties close to the best ever achieved using low-fluorine CSD with preformed nanocrystals in terms of self-field J_c, in-field J_c, angular dependence of J_c and pinning force density (F_p).[14-15, 17, 25, 29] CSD of low-fluorine YBCO solutions with preformed double metal oxide nanocrystals is presented as a powerful method to fabricate high performance superconductors with enhanced pinning properties in applied magnetic fields, which is ready for its use in the fabrication of nano-added coated conductors.

Experimental

Preformed nanocrystals synthesis and characterization

Batches of four types of double metal oxide nanocrystals with perovskite structure—BZO, BHO, BTO, and SZO—were synthesized via microwave-assisted solvothermal method. The reaction starts from bimetallic organometallic precursors incorporated in an ethanol solution under inert gas conditions. The samples were subjected to microwave radiation at 160 °C for 30 minutes at a maximum output of 300W in a CEM Discover SP Microwave. The as-synthesized nanocrystals were purified and stabilized with the minimum required amount of 2-[2-(2-methoxyethoxy)ethoxy]acetic acid (MEEAA, Aldrich, technical grade ≥ 90%) in methanol (Carl-Roth, 99.9%). The final concentration of the nanosuspension was measured by Thermogravimetric Analysis (TGA, Netzsch STA 449E3 Jupiter).

The phase composition of the as-synthesized nanocrystals was analysed by powder X-ray diffraction (XRD, Thermo Scientific ARL XTra diffractometer) using Cu K_α radiation. The morphology and size of the nanocrystals in the stable suspension were studied by Transmission Electron Microscopy (TEM, JEOL JEM-2000FS operated at 200 kV with C_s corrector). The diameter of the nanocrystals was determined from the TEM images using the software *ImageJ* and measuring at least 200 particles. The solvodynamic diameter was measured by Dynamic Light Scattering (DLS, Marlvern Nano ZS) with backscatter detection (scattering angle 173°).

Nanocomposite formation

Low-fluorine YBCO precursor solutions were prepared by dissolving Y-propionate, Ba-TFA, and Cu-propionate in an Y:Ba:Cu ratio of 1:2:3 in methanol (CHROMASOLV, ≥99.9% - Sigma-Aldrich). All precursor solutions have a total metal ion concentration of 1.08 M. For preparing the four nanocomposite precursor solutions with a 5 mol% load of nanocrystals, adequate amounts of colloidal nanosuspensions were added to the pristine YBCO precursor solution. Unlike in previous works where a ligand exchange is needed[15, 17], the nanosuspensions can be directly added with a micropipette to the YBCO precursor solution without the need of a ligand exchange, as the use of MEEAA guarantees that the colloidal stability of the nanocrystals is maintained in the highly ionic YBCO precursor solution. These precursor solutions were deposited on (100) LAO (CrysTech GmbH) single crystal substrates via spin-coating at 2000 rpm for 1 minute and pyrolyzed by heating to 400 °C in wet oxygen atmosphere with a heating rate of 1-5 °C/min to remove the organics. After pyrolysis, the as-deposited coatings were crystallized according to Rijckaert *et al.*[29] with a two-step process consisting of dwelling at 640 °C for 60 min and a dwelling at 810 °C for 70 min both in a humid 100 ppm O_2 in N_2 atmosphere injected at a flow rate of 1 L/min by bubbling the dry gas through deionized water at room temperature. The process is illustrated in the SI, Figure S2 . Finally, the film was annealed at 450 °C for 2 hours in pure O_2 atmosphere and quenched to room temperature to obtain the superconducting YBCO phase. Three samples of each type of nanocomposite were grown in order to check the reproducibility of the results.

Characterization of the films

The phase composition and the texture of the fully converted YBCO layers were analysed by XRD using a D4 ENDEAVOR diffractometer (Bruker; Cu-K_α radiation) with a 3-axis goniometer. To account for the LAO substrate miscut angle, the specimens were aligned by maximizing the intensity of 005 peak of YBCO with respect to the in-plane (φ) and out-of-plane

(ω) orientations via measurements of 005 rocking curves at various φ. In the regions of LAO reflections, XRD patterns were measured at a factor of 20 smaller intensity of the incident beam (not shown). The lattice parameter *c* of YBCO was assessed from the peak positions of all 00ℓ reflections (ℓ = 1 to 14) and using pseudocubic lattice parameter of LAO (3.79077 ± 0.00005 Å) as an internal standard[30]. The microstrain was assessed from the integral breadths (β) of YBCO $K_{\alpha 1}$ 00ℓ peaks following the Williamson-Hall approach as described by Scardi *et al.*[31] Namely, the reciprocal integral breadths $\beta^* = 2\,\beta\lambda\cos\theta$ (λ is the wavelength, θ is the Bragg angle) were plotted as a function of the reciprocal spacing $d^* = 2\sin\theta/\lambda$ and fit with a linear function $\beta^* = 1/L_{00\ell} + 2\varepsilon_{00\ell}$ yielding the average crystalline size ($L_{00\ell}$) and the microstrain ($\varepsilon_{00\ell}$) along the *c*-axis. The epitaxial fraction (*EF*)—the ratio of epitaxial YBCO to the total amount of material in the film—was assessed by comparing the spatially and over 2θ integrated intensity of the 005 reflection of the YBCO film under study with the similar data for a standard (005 reflection of the 200 ± 10 nm thick pulsed laser deposited-YBCO film) as described in detail by Rikel *et al.*[32-33] The out-of-plane texture ($\Delta\omega$) was quantified by analysing the full width at half maximum of 005 peak of YBCO.

The microstructure of the films as well as their thickness were investigated using high resolution and scanning transmission electron microscopy (HRTEM and STEM) via a C_s-corrected JEOL JEM 2200-FS instrument operated at 200 kV with bright field (BF) detectors. Cross-sectional view TEM lamellae were prepared via the Focused Ion Beam (FIB) technique in a FEI Nova 600 Nanolab Dual Beam microscope. The lamellae were extracted using the *in situ* lift-out procedure with an Omniprobe extraction needle. The software *ImageJ* was used to measure the average diameter of the nanoparticles in the YBCO matrix from several cross-sectional images using at least 150 nanoparticles per sample.

The self-field J_c was inductively measured in liquid nitrogen at 77 K using a Theva Cryoscan system with a voltage criterion of 50 μV. Transport current measurements were made in a four-probe configuration on bridges of 800 μm length and 50 μm width prepared by wet chemical etching. The magnetic field dependence (up to 14 T) of transport J_c was measured at 30, 50 and 77 K with a Quantum Design Physical Property Measurement System using an electric field criterion of 1 μV/cm. The critical temperature (T_c) was defined as the temperature at which the resistivity (ρ) was 50% of the normal state resistivity at 95 K ($\rho(T_c) = 0.5 \cdot \rho(95\ K)$) and the accommodation field (H^*) as the field at which the J_c was 90% of the self-field J_c ($J_c(H^*) = 0.9 \cdot J_{c0}$). The exponent α was obtained by fitting the so-called collective vortex pinning region of the J_c(H) plot at 77 K (between H* and 0.5 T) to the power-law $J_c = A(T) \cdot H^{-\alpha}$, The angular dependence of J_c was measured under maximum Lorentz force configuration (*i.e.* with the magnetic field perpendicular to the direction of the transport current) with an angle resolution of 1º near the *c*- and *ab*-axis and 5º otherwise; the measurements were done at 77 K and 1 T, 50 K and 3 T and 30 K and 14 T.

Results and discussion

Double metal oxide nanocrystals synthesis

The as-synthesized BZO, SZO, BHO and BTO nanoparticles show XRD patterns characteristic of nanocrystalline materials (Figure 1A). They can be indexed assuming pseudocubic structure, but the line breadths can be affected by tetragonal (for BTO) and orthorhombic (for SZO) distortions. The pseudocubic lattice parameters 4.18 ± 0.02 Å (BZO), 4.11 ± 0.01 Å (SZO), 4.23 ±0.02 Å (BHO) and 4.00 ± 0.01 Å (BTO) are all larger than the pseudocubic lattice parameter of YBCO. As in the works of Obradors *et al.*[21] and Li *et al.*[22], small peaks at 2θ = 24, 34° of $BaCO_3$ impurity phase are seen for BHO and BZO powders. After the addition of the ligand MEEAA, the nanosuspensions in polar solvent (*e.g.* methanol) are stable and remain agglomeration-free for months (See SI, Figure S3). The DLS analysis of the stable

nanosuspensions show solvodynamic diameters of 4.9 ± 1.9 nm for BZO, 7.6 ± 2.3 nm for SZO, 4.1 ± 1.1 nm for BHO and 8.1 ± 3.1 nm for BTO nanocrystals (Figure 1B). The TEM images (Figures 1D to 2G) confirm the presence of agglomeration-free nanocrystals with diameters of 3.3 ± 0.4, 5.9 ± 0.6, 2.9 ± 0.4, 6.1 ± 0.8 nm as well as their crystallinity (insets of Figures 1D to 2G). The 1-2 nm difference between TEM and DLS measurements corresponds to the ligand and the solvation shell.

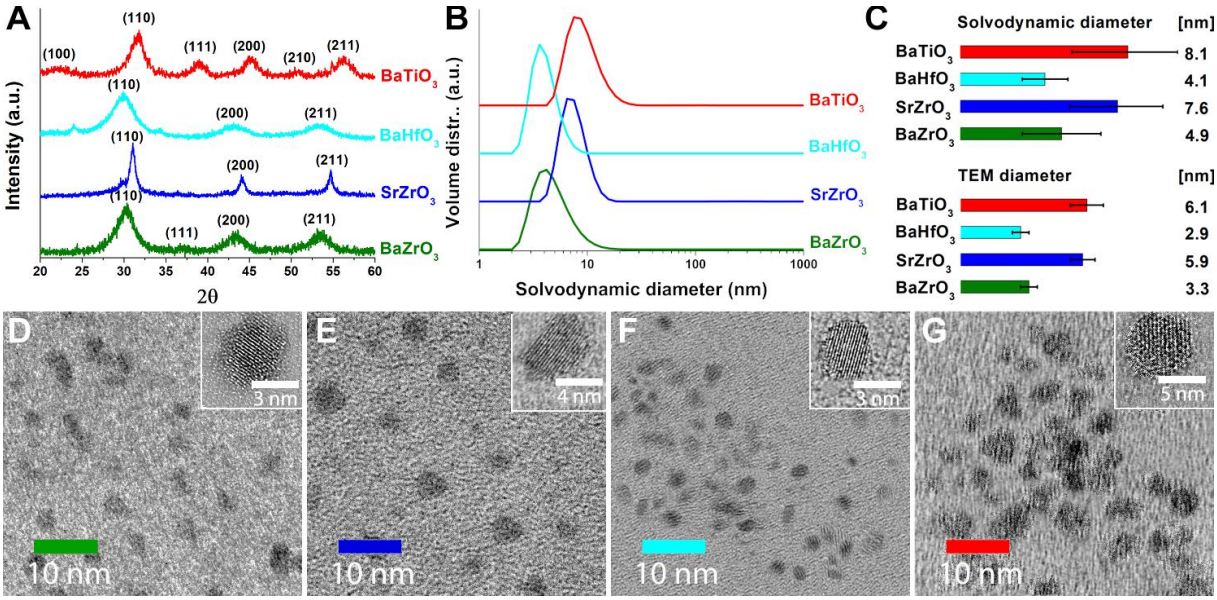

Figure 1: (A) XRD patterns of as-synthesized nanocrystals indexed using pseudocubic crystalline structure. (B) DLS volume plots showing the monodisperse and agglomeration-free nanosuspensions. (C) Solvodynamic diameter and TEM diameter of the different nanocrystals. (D-G) TEM images of BZO (D), SZO (E), BHO (F) and BTO (G) nanocrystals showing no agglomeration with detail of a single nanocrystal in inset.

Structural analysis of nanocomposite film

Figure 2 shows the ω-2θ XRD patterns between 5 and 74° for a pristine YBCO film and four different YBCO nanocomposites containing 5 mol% of BZO, SZO, BHO, and BTO, nanocrystals, respectively (see SI, Figure S4, for XRD patterns between 5 and 145°). 00ℓ reflections (ℓ = 1, 2, …, 14) of YBCO are clearly seen in the XRD patterns. Some reflections of secondary phases can also be identified, such as $Y_2Ba_4Cu_7O_{15}$ (Y247), $YBa_2Cu_4O_8$ (Y124), $Y_2Cu_2O_5$ and Y_2O_3. All nanocomposites show a reduction of the Y247 phase (2θ = 7.0, 14.0, 24.6, 27.9, 31.8, 39.1, 42.0, 46.6, 54.3, 58.3°) when compared to the pristine film. The addition

of BTO nanocrystals causes formation of Y124 inclusions, not seen in other films, while the nanocomposite with SZO nanocrystals shows much higher amount of Y_2O_3 than the other films. Analysis of the centroid positions of 00ℓ lines and line broadening effects similar to that done by Rikel and Hellstrom[34] for $Bi_2Sr_2CaCu_2O_{8+x}$ showed that the YBCO phase in all the films contains less than 0.2% of Y124 intergrowth defects also known as extended stacking faults[35-37].

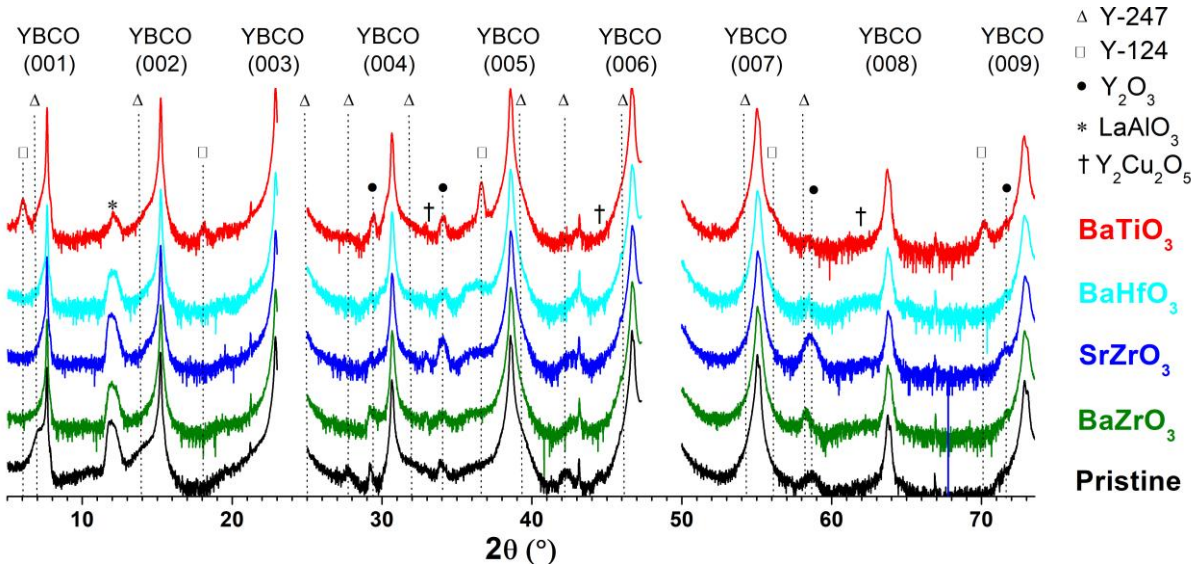

Figure 2: Offset-coupled ω-2θ scan (log-scale) of pristine and 5 mol% nanocrystal-containing films between 5 and 74°. The regions of epitaxial LAO reflections were measured at smaller intensity of incident beam (not shown). Indexing of peaks is based on the data of Koblichka-Veneva *et al.*[38]; Power Diffraction Files for Y_2O_3 (74-0553) and $Y_2Cu_2O_5$ (78-2100), and Qu *et al.*[39] for LAO peak at $2\theta = 12.2°$. The small peaks at $2\theta \sim 22, 43, 67°$ correspond to LAO reflections caused by secondary radiation of the X-ray tube due to impurities.

Table 1 summarizes the results of XRD studies (lattice parameter *c*, microstrain ($\varepsilon_{00\ell}$), out-of-plane texture ($\Delta\omega$), epitaxial fraction (*EF*) of YBCO), inductive J_c (77K, self-field) measurements, and TEM results on the film thickness. In comparison with the pristine film, the lattice parameter *c* increases in BZO and BHO nanocomposites while decreases in SZO and BTO nanocomposites. Line broadening analysis showed that in all films, the average crystallite size $L_{00\ell}$ coincides within the 10-30% error with the YBCO layer thickness assessed from TEM. Addition of BZO, SZO and BHO nanocrystals strongly increases $\varepsilon_{00\ell}$, whereas the BTO-containing film has slightly lower $\varepsilon_{00\ell}$. Moreover, compared to the pristine film, $\Delta\omega$ values are about 50% larger in BZO, SZO and BHO nanocomposites and 15% lower in BTO

nanocomposite. Deterioration of out-of-plane texture in the BZO and BHO nanocomposites is not accompanied by changes in epitaxial fraction. The *EF* values are very similar in all films, except for SZO nanocomposite. The error in EF is relatively large mainly due to uncertainties in thickness, and the values are likely slightly underestimated by the worse quality of YBCO at the edges of the film. As the Cryoscan measurements show that the edge effects are similar in all samples, we may conclude from comparison of EF values that incorporation of BZO, BHO and BTO nanocrystals is not detrimental for the epitaxial growth of YBCO. BZO, BHO and BTO nanocomposites show self-field J_c values of 4.7, 4.5, and 4.6 MA/cm^2 respectively, which are even slightly higher than the 4.2 MA/cm^2 of the pristine sample. The low standard deviations of the measurements of three samples per nanocomposite confirm the reproducibility of these results. The correlation between *EF* and J_c cannot be confirmed due to significant errors in assessing *EF*. Such a correlation, however, is very plausible. The SZO nanocomposite shows 21±8% reduced *EF* and 35±7% reduced self-field J_c. It is thus likely that incorporation of SZO nanocrystals suppresses J_c by hindering the epitaxial growth of YBCO.

Table 1: YBCO lattice parameter (c), microstrain ($\varepsilon_{00\ell}$), out-of-plane texture ($\Delta\omega$), epitaxial fraction (EF), inductive self-field critical current density at 77 K (J_c), and thickness (t) of pristine and nanocomposite YBCO films (numbers in parentheses show the error in the last digit).

Sample	c (Å)	$\varepsilon_{00\ell}$ (%)	$\Delta\omega$ (°)	EF (%)	J_c (MA/cm^2)	t (nm)
Pristine	11.6786 (2)	0.083 (3)	0.427 (2)	79 (8)	4.2 (2)	300 (20)
BZO	11.6811 (2)	0.138 (3)	0.589 (3)	79 (6)	4.7 (3)	260 (20)
SZO	11.6758 (4)	0.155 (3)	0.687 (4)	63 (5)	2.7 (2)	290 (20)
BHO	11.6818 (3)	0.166 (4)	0.585 (3)	75 (6)	4.5 (2)	240 (20)
BTO	11.6737 (2)	0.071 (4)	0.369 (2)	78 (7)	4.6 (3)	300 (20)

The nanoparticle distribution within the YBCO matrix and the presence of secondary phases and structural defects were studied by BF-STEM. The pristine YBCO film (Figure 3A) shows a low amount of secondary phases and structural defects such as intergrowths. The twin

boundaries formed upon the tetragonal-to-orthorhombic transition that takes place during the oxygenation treatment[40] are highly coherent being parallel to the *c*-axis and forming almost periodic pattern in the *ab*-plane. BF-HRTEM shows good (00ℓ) texture at the YBCO/LAO interface and the selected area diffraction pattern confirms the excellent epitaxial growth (see SI, Figure S5). The BZO nanocomposite (Figures 3B and 3E) shows a homogeneous spatial distribution of nanoparticles. The nanoparticle size distribution has an average diameter $\langle d \rangle$ = 10 nm and mean square deviation σ_d = 6 nm. In addition to nanoparticles, a rather high concentration of planar defects is visible throughout the whole layer. Based on the previous studies[41-43], these planar defects are short Y124 intergrowth or stacking fault defects consisting on an extra Cu-O plane with a finite lateral extension surrounded by partial dislocations that enhance the microstrain of the YBCO lattice. It is known that the presence of nanoparticles with a high lattice mismatch with the YBCO matrix generates multiple stacking faults that may even form ordered arrays of Y124 phase[41]. Another important feature that can be clearly seen in the STEM images of the BZO nanocomposite is the decrease in the coherence of the twin boundaries along the *c*-axis (see SI, Figure S6 for larger view TEM images). As previously reported[15, 44], the presence of nanocrystals, secondary phases and planar defects often result in a loss of twin boundary coherence. The SZO nanocomposite (Figures 3C and 3F) also shows a homogeneous distribution of SZO nanoparticles and a decrease in the coherence of the twin boundaries. The nanoparticle distribution has a slightly larger mean diameter, $\langle d \rangle$ = 12 nm and σ_d = 6 nm, and the nanocomposite shows a smaller density of planar defects. In agreement with XRD data (Figure 2) a larger amount of secondary phases, mainly Y_2O_3 particles, is observed. The 30 to 60 nm large second–phase particles are randomly distributed, likely causing the reduced EF and J_c of the SZO nanocomposite. The BHO nanocomposite (Figures 3D and 3G) shows a homogeneous distribution of nanoparticles with $\langle d \rangle$ = 7 and σ_d = 4 nm. It also shows the highest concentration of planar defects and a drastic reduction of the twin boundary

coherence along the *c*-axis. Conversely. the BTO-added YBCO film (Figure 3H) does not show individual nanoparticles, but only a few large agglomerations of BTO 100-200 nm in size. Large Y124 inclusions can be seen at the YBCO/LAO interface and on the surface of the YBCO layer, which is consistent with XRD observations (Figure 2). The rest of the film is strongly textured, with highly coherent twin boundaries and very low concentration of other defects; only a few Y124 planar defects surrounding the large BTO clusters were observed. The aggregation of nanoparticles seen in the BTO-added film, has been observed in previous works using different preformed nanocrystals such as ZrO_2, CeO_2 or Au[15-19]. The reason why BTO nanocrystals tend to agglomerate while BZO, SZO and BHO remain homogeneously distributed with only moderate coarsening is unclear, and will be studied in a future work.

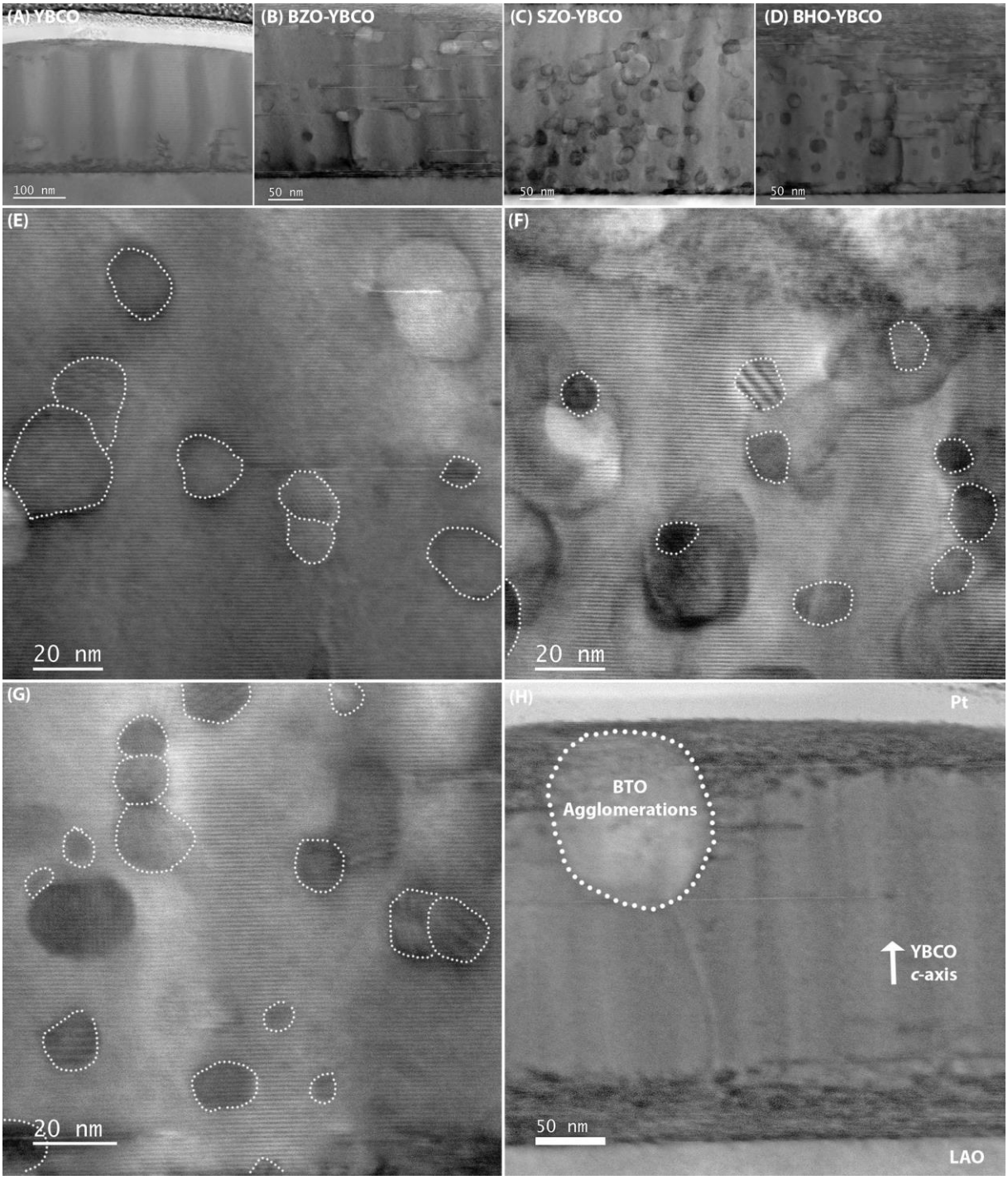

Figure 3: BF-STEM images of: (A) pristine YBCO film with highly coherent twin boundaries, some intergrowths at the YBCO/LAO interface and low amount of other defects and secondary phases; (B, E) BZO nanocomposite showing a homogeneous distribution of BZO nanoparticles ($\langle d \rangle$ = 10 nm, σ_d = 6 nm), a high concentration of planar defects and reduced twin boundary coherence; (C, F) SZO nanocomposite with homogeneous distribution of SZO nanoparticles ($\langle d \rangle$ = 12 nm, σ_d = 6 nm), large amount of secondary phases, mainly Y_2O_3, and reduced twin boundary coherence; (D, G) BHO nanocomposite with homogeneous distribution of BHO nanoparticles ($\langle d \rangle$ = 7 nm, σ_d = 4 nm), a very high density of planar defects and a drastic decrease in twin boundary coherence; (H) BTO-added YBCO film showing big agglomerations of BTO without individual nanoparticles, large Y124 inclusions at the YBCO/LAO interface and on the surface of the YBCO film and highly coherent twin boundaries.

The size distributions of the nanoparticles in the YBCO matrix are plotted in Figure S7 of the SI and summarized in Table 2 together with the initial diameter of the nanocrystals, the coarsening factor and the density of nanoparticles in the film. In BZO, SZO and BHO nanocomposites there is some coarsening of the nanocrystals, by a factor of 2 to 3 with respect to the initial size, most likely due to grain coalescence during the high-temperature thermal processing of the films.[45] However, this coarsening does not disturb the epitaxial growth of YBCO (Table 1) and the final size of the nanocrystals is rather small compared to previous studies. Remarkably, the average diameter of BHO nanocrystals in the YBCO layer (7 nm) is among the smallest ever achieved for artificial pinning centres in CSD[11-21, 25, 29, 46] despite the lack of a seed layer. Only the Y_2O_3 nanoparticles spontaneously segregated from yttrium-excess YBCO solutions in the work of Lei *et al.*[13] have a smaller average diameter of 5.6 nm. Smaller sized nanoparticles result in a higher number of nanoparticles in the layer (which in turn, induce more planar defects). Therefore, more pinning sites are present and stronger pinning enhancement is expected. Overall, the above observations confirm our earlier result that the two-step crystallization process improves YBCO texture in nanocomposites[29] and nanocrystal distribution in BZO, SZO and BHO nanocomposites, eliminating the need of using a seed layer. BHO nanocomposite contains the smallest and, therefore, the most numerous nanoparticles (Table 2). In addition, because of the largest lattice mismatch, BHO nanoparticles in the YBCO matrix should lead to the largest strain effects and, as a consequence, to the highest density of Y124 planar defects, whose formation releases the elastic energy around the nanoparticles.[41] This explains why BHO has the highest $\mathcal{E}_{00\ell}$. The BZO nanocomposite has larger nanoparticles (10 nm) which have a smaller mismatch with YBCO; therefore, the $\mathcal{E}_{00\ell}$ increase is not as pronounced as in BHO. SZO nanoparticles are even bigger (12 nm) and have the lattice mismatch with the YBCO matrix smaller than BZO. However, the high value of $\mathcal{E}_{00\ell}$ observed in this nanocomposite can be related to presence of a large amount of Y_2O_3 nanoparticles[13]. The

BTO-added film contains no individual nanoparticles and therefore has a similar $\mathcal{E}_{00\ell}$ as the pristine YBCO.

Note that the above considerations are based on the assumption that inhomogeneity in oxygen distribution that may also affect $\mathcal{E}_{00\ell}$ is the same in all films, which could be not the case as low-temperature oxygenation kinetics is strongly affected by the presence of nanoparticles[47].

Table 2: Summary of the diameter of the different nanoparticles in the colloidal solution and in the YBCO matrix, the calculated coarsening factor, and the number density of nanoparticles in the YBCO film.

Type of nanoparticle	Diameter in solution (nm)	Diameter in YBCO matrix (nm)	Coarsening factor	Density of nanoparticles ($\times 10^3$ μm^{-3})
BZO	3.3 ± 0.4	10 ± 6	3.0	46 ± 8
SZO	5.9 ± 0.6	12 ± 6	2.0	21 ± 9
BHO	2.9 ± 0.4	7 ± 4	2.4	113 ± 7
BTO	6.1 ± 0.8	100 - 200	-	-

Field-dependence of J_c

Figure 4A shows the dependence of transport J_c on an external magnetic field for the pristine YBCO film and the four nanocomposites at temperatures of 30, 50 and 77 K. The normalized values of J_c with respect to the self-field value are also included (Figure 4B) to show the relative J_c decay. BZO, SZO and BHO nanocomposites exhibit a much slower decay of J_c compared to the pristine YBCO film, as opposed to the BTO-added film which shows faster J_c decay. In the SZO nanocomposite the J_c at low magnetic fields up to 0.1 T is lower than in the pristine YBCO film due to the initial low self-field J_c (see Table 1), while slightly better in stronger fields (H > 0.1 T). However, the normalized J_c shows that the pinning properties are strongly enhanced compared to the pristine film in the same way as in BHO and BZO nanocomposites. Therefore, improving the self-field J_c of the SZO nanocomposite by improving the epitaxial growth of YBCO could lead to a nanocomposite with excellent in-field properties. In comparison the BZO and BHO nanocomposites have self-field J_c even slightly better than the pristine film (Table 1)

and behave much better in the presence of an external magnetic field at all temperatures, with the BHO nanocomposite being the clear champion both in absolute and normalized values. Table 3 compares the J_c values of the different films in an applied magnetic field of 1 T at three measurement temperatures, showing the BHO nanocomposite J_c values approximately 3 to 3.5 times higher than the pristine film. Comparatively, the BZO nanocomposite shows an improved J_c by a factor of 2 to 2.5. The accommodation field H^*, also presented in Table 3, shows that the single vortex pinning region is enhanced by the addition of nanocrystals from the initial 4 mT in the pristine film to 17, 19 and 20 mT in the BZO, SZO and BHO nanocomposites, respectively. However, the BTO-added YBCO film shows the same H^* as the pristine film. The fact that the single vortex pinning regime is not affected in this film is a reasonable consequence of the agglomeration of BTO nanocrystals (Figure 3H). The exponent α, obtained by fitting the so-called collective vortex pinning region to the power-law $J_c = A(T) \cdot H^{-\alpha}$, shows a pronounced decrease for SZO, BZO and BHO nanocomposites. This corresponds to a slower decay of J_c with the magnetic field. T_c is reduced by the addition of SZO and BHO nanocrystals. T_c suppression in YBCO films with high $\mathcal{E}_{00\ell}$ has been observed in previous works[48-49]. However, our data on T_c do not fully follow this trend, suggesting importance of other factors. Nonetheless, the BTO-added film has even higher T_c than the pristine film, which is in accord with lower $\mathcal{E}_{00\ell}$.

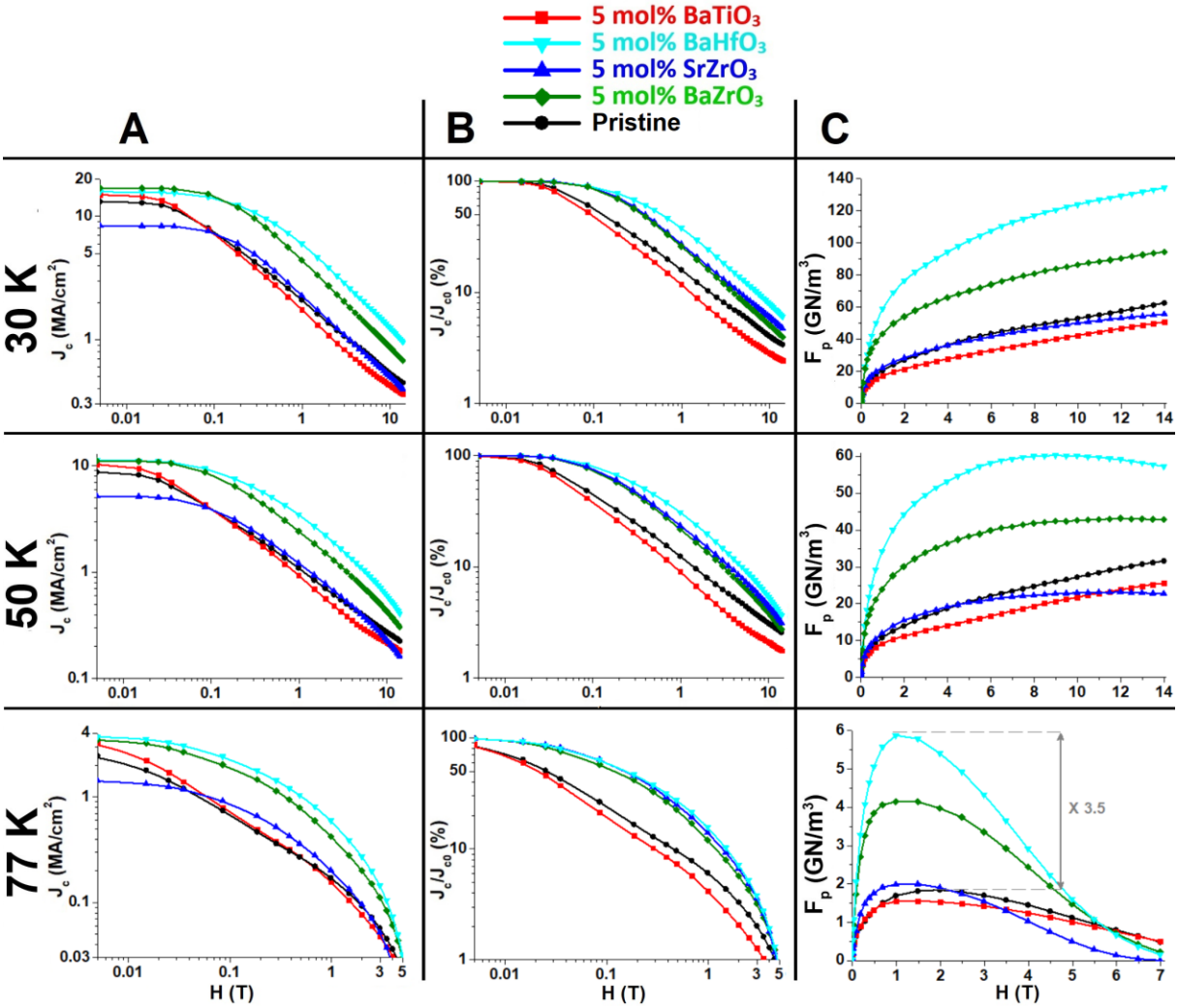

Figure 4: (A) Field dependence of transport J_c in absolute value and (B) normalized with respect to the self-field J_c, and (C) F_p versus magnetic field, at 30 K, 50 K and 77 K. The BHO nanocomposite shows the best performance at all temperatures reaching 3.5 times higher pinning forces than the pristine film at 77 K and 1 T.

Table 3: Accommodation field (H^*) and power-law exponent (α) at 77 K; critical current density (J_c) in absolute and normalized values at 77, 50 and 30 K in an external magnetic field of 1 T, and critical temperature (T_c) of the films.

Sample	77K		77 K, 1 T		50 K, 1 T		30 K, 1 T		
	H^* (mT)	α	J_c (kA/cm^2)	J_c / J_{c0} (%)	J_c (kA/cm^2)	J_c / J_{c0} (%)	J_c (kA/cm^2)	J_c / J_{c0} (%)	T_c (K)
Pristine	4	0.53	175	6	1145	12	2197	16	91.3
BZO	17	0.38	421	12	2431	22	4415	26	91.3
SZO	19	0.35	202	14	1214	24	2276	27	90.2
BHO	20	0.33	595	16	3477	31	5990	38	90.7
BTO	4	0.60	170	4	1010	9	1906	12	92.3

The pinning force density (F_p) is also enhanced by the addition of certain nanocrystals. Figure 4C shows the F_p values corresponding to the J_c data in Figure 4A, clearly indicating the pinning

enhancement by BZO and BHO nanoparticles. The BHO nanocomposite has the best F_p of 5.9 GN/m^3 at 77 K in 1 T compared to 1.7 GN/m^3 of the pristine film. This means that F_p is increased by a factor of 3.5 in the BHO nanocomposite. The nanocomposite films have the maximum F_p at 77 K at a magnetic field of ~1 T while in the pristine layer the maximum is at a magnetic field of ~2 T. At 77 K, F_p is enhanced for magnetic fields up to 5.5 T while at 30 and 50 K it is enhanced in the whole range of measured magnetic fields. The maximum F_p (5.9 GN/m^3) of the BHO nanocomposite compares favourably to previous YBCO films with preformed BHO and BZO nanocrystals[21-22] (with maximum pinning forces between 2.2 and 4.5 GN/m^3) despite the much higher nanocrystal load used in these works (20 mol%) and the use of all-TFA YBCO inks. It also compares favourably to YBCO films with *in situ* formation of pinning centers deposited by low-fluorine CSD such as a 5 mol% BZO-YBCO[50](4.6 GN/m^3), a 10 mol% BZO-YBCO[51] (3.8 GN/m^3) or a 12 mol% BHO-YBCO film[11] (4.1 GN/m^3). However, it is still far from the record F_p values of *in situ* YBCO films grown by the all-TFA route (22 GN/m^3 in a 10 mol% BZO-YBCO film[14])

Angular dependence of J_c

For all films and all measurement conditions, the angular dependence of J_c (Figure 5) shows a typical sharp increase of J_c when the external magnetic field is parallel to the *ab*-planes (θ = 90º). This effect is caused by the electronic anisotropy, the intrinsic pinning of the layered crystal structure, and defects in the *ab*-plane such as intergrowths or dislocations.[52-55] In the BZO and BHO nanocomposites there is an overall increase of the absolute J_c due to the isotropic pinning produced by the spherical and homogeneously distributed nanocrystals, and a broadening of the *ab*-peak caused by the high concentration of Y124 planar defects produced by these nanocrystals and their corresponding dislocations (Figure 3B and 3D).[41-43] This results in a more isotropic behaviour over the whole angular range. The difference compared to the pristine film is especially dramatic at 77 K and 1 T, where J_c at intermediate angles is 4 to 6

times higher in the BHO nanocomposite than in the pristine film. The overall increase of J_c is higher in BHO-nanocomposite, because BHO nanocrystals are smaller and less agglomerated which translates into a higher density of pinning sites (Table 2). The anisotropy factor *A*—defined as the ratio between the maximum and the minimum in the $J_c(\theta)$ plot—changes from 3.5 in the pristine film to 2.3 in the BZO and 1.5 in the BHO nanocomposites at 77 K. The SZO nanocomposite also shows more isotropic behaviour in all measured conditions due to the enhanced pinning (A = 2.1). However, its performance is limited by the low self-field J_c and T_c caused by the poor YBCO growth in this nanocomposite. The BTO-added YBCO film shows no overall increase of J_c due to the lack of isotropic pinning sites[52] (Figure 3H) but shows strong *ab*-peaks (especially at 77 K and 1 T) that rapidly decreases when the magnetic field is not parallel to the *ab*-direction, leading to anisotropy (A = 6.9) almost twice larger than in the pristine film. This suggests that the increase in the *ab*-peaks is due to the enhancement of intrinsic pinning due to about 15% sharper out-of-plane texture in this film (see Table 1).

Several features in the angular dependence of J_c of the different nanocomposites can be seen at varying temperature and magnetic field. At 77 K and 1 T, the BHO nanocomposite shows shoulders close to the *ab*-peak that disappear at lower temperatures. These shoulders have been frequently reported in films with strong pinning at small, sparsely distributed, random defects at high temperature[56-59] and explained by Paturi *et al.*[60] in the context of the vortex path model[61-62]. For higher fields and low temperatures, the *ab*-peaks narrow since the intrinsic pinning of YBCO Cu-O planes dominates over the pinning caused by the intergrowth defects.[52, 63] The BTO-added film as well as the pristine film exhibit a small *c*-axis peak at 77 K and 1 T caused by the pinning at highly coherent twin boundaries. This *c*-axis peak disappears for medium magnetic fields and temperatures (50 K, 3 T) and evolves to a dip at even higher fields and lower temperatures (30 K, 14 T) due to vortex channelling effects.[64] This vortex channelling occurs along highly coherent twin boundaries only near $\theta = 0^{o}$ and at low temperatures[64-66].

However, in the films with homogeneously distributed nanocrystals and a high density of Y124 intergrowth defects (BZO, BHO, SZO) and/or secondary phases (SZO), the vertical coherence of twin boundaries is reduced[15, 44] (Figure 3) and vortex channelling is prevented[66]. This eliminates J_c suppression, which explains why the *c*-axis dip is only visible in the pristine and the BTO nanocomposite. In the nanocomposites with strong pinning enhancement (BHO, BZO and SZO nanocomposites) the *c*-axis peak is not visible at low magnetic fields and high temperatures (77 K, 1 T), due to the lower coherence of the twin boundaries.[43] At 50 K and 3 T, a small *c*-axis peak appears and then disappears again at 30 K and 14 T. The collapse of the *c*-axis peak at low temperatures has been explained by Yamasaki *et al.*[67] as a consequence of the strong intrinsic pinning of the YBCO layered structure at low temperatures.

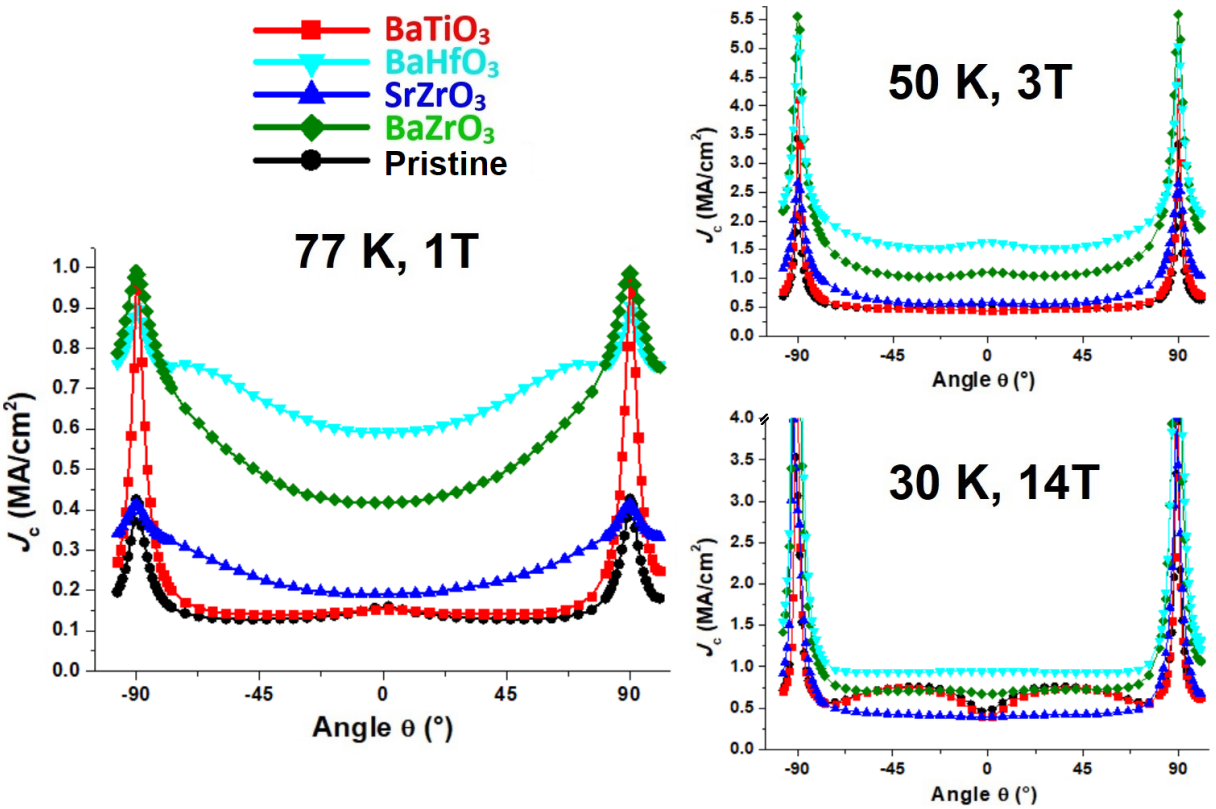

Figure 5: Angular dependence of J_c at 77 K and 1 T; 50 K and 3 T and 30 K and 14 T. Nanocomposite films, with the exception of BTO, show a much more isotropic behaviour with the BHO nanocomposite being the best performing at all temperatures. Data near $\theta = \pm 90^{o}$ at 30 K and 14 T not shown due to heating effects.

Therefore, the difference in the shape of the $J_c(\theta)$ plots, *i.e.* the difference in pinning ability depending on the direction of the magnetic field, is a result of the different microstructure of

the nanocomposites. Figure 6 schematically illustrates this difference, depicting the main type of defects present in each nanocomposite and the direction of movement of the magnetic vortices given by the Lorentz Force ($\overrightarrow{F_L} = \vec{J} \times \vec{H}$).

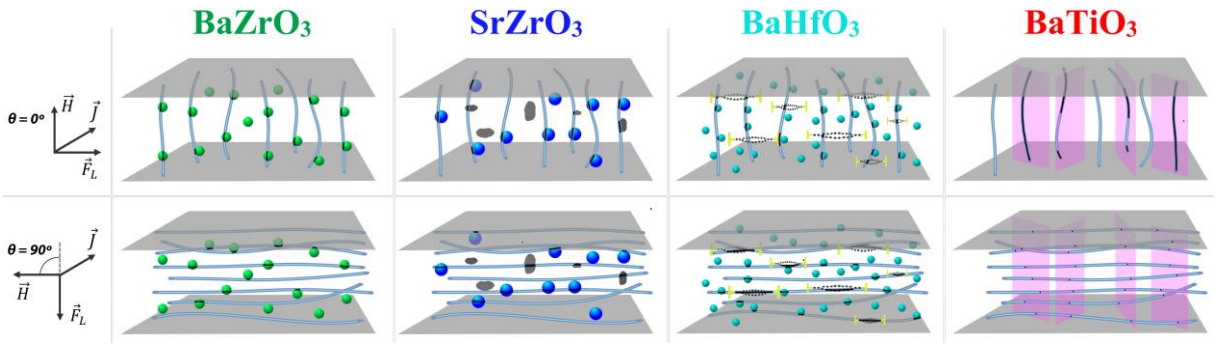

Figure 6: Schematic illustration of the four nanocomposites showing the main defects present: Homogeneously distributed nanocrystals (for BZO (green), SZO (blue) and BHO (cyan)), intergrowths (for BHO), small secondary phases such as Y_2O_3 (for SZO (grey)) and highly coherent twin boundaries (for BTO (pink)). These defects have a different *pinning length* (in black) depending on the direction of the magnetic field, which gives rise to the different $J_c(\theta)$ plots. The magnetic field is always perpendicular to the direction of the transport current and the angle θ is defined as 0º when the magnetic field is parallel to the YBCO *c*-axis. The magnetic vortices and their direction of movement given by the Lorentz Force are also represented.

Relation between microstrain and pinning properties

Introducing different nanocrystals in YBCO leads to important differences in the microstructure, such as size and number density of nanoparticles, strain fields around nanoparticles due to lattice mismatch with YBCO, planar defects (e.g., Y124 intergrowth defects surrounded by dislocation loops) that are induced by plastic deformation of the matrix in the vicinity of nanoparticles, secondary phase particles, and twin boundaries with different extent of *c*-axis coherence. Detailed analysis of these differences is beyond the scope of the present work. However, it is possible to correlate pinning properties with such a generalized characteristic of the microstructure as the microstrain. The introduction of nanocrystals in YBCO results in an increase in $\mathcal{E}_{00\ell}$ when they are homogeneously distributed throughout the layer (Table 1), and this in turn can be related to the enhanced pinning properties and J_c isotropy as previously reported by other groups.[12, 15, 17, 41-43, 68-69] The increase of $\mathcal{E}_{00\ell}$ in the BZO, SZO and BHO nanocomposites results in a nearly linear increase of H^* (Figure 7A) and a polynomial

decrease of α (Figure 7B) at 77 K. Conversely, the BTO-added film has $\mathcal{E}_{00\ell}$ similar to the pristine film due to the agglomeration of BTO nanocrystals and therefore shows no improvement of pinning properties. Figure 7C shows a linear correlation between $\mathcal{E}_{00\ell}$ and the normalized J_c at 77K and 1 T as a consequence of the enhanced pinning properties.

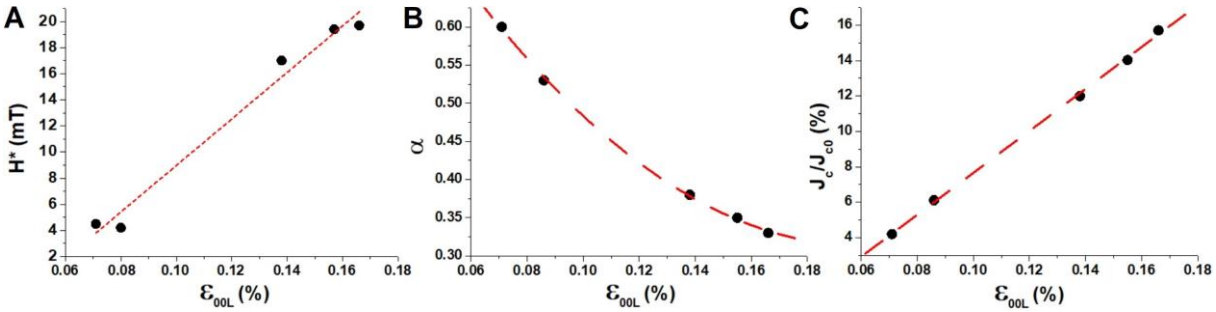

Figure 7: Correlation among the pinning properties—(A) Accommodation field (H^*), (B) power-law exponent α, and (C) normalized J_c at 1 T—and the microstrain ($\mathcal{E}_{00\ell}$) at 77 K. H^* and the normalized J_c at 1T show a nearly linear correlation with $\mathcal{E}_{00\ell}$ while α shows a polynomial decrease with $\mathcal{E}_{00\ell}$.

Conclusions

YBCO nanocomposites on LAO single-crystalline substrates were fabricated via CSD from colloidal low-fluorine YBCO inks containing different preformed double oxide nanocrystals (3-6 nm in diameter). The separate preparation of the nanocrystal colloidal solutions allows great control over size, shape, crystallinity and concentration of the nanocrystals and therefore over the final microstructure of the YBCO nanocomposites, while the preparation of low-fluorine YBCO inks allows for a more environment-friendly process. Four types of nanocomposites containing BZO, SZO, BHO and BTO nanocrystals were grown to study the influence of nanocrystal composition on the final superconducting properties. All films were crystallized under the same thermal treatment. No seed layer was needed since BZO, SZO and BHO nanocrystals remain homogeneously distributed with only minor coarsening, facilitating upscaling in future work. The defect landscapes of the nanocomposites were compared and the YBCO microstrain of the films was measured and related with the accommodation field and the power-law exponent α. The addition of BZO, SZO and BHO nanocrystals increases the microstrain of the YBCO matrix and this in turn causes a strong enhancement of the pinning

properties, while BTO nanocrystals cluster and no enhancement occurs. The SZO nanocomposite shows enhanced microstrain and good pinning properties but reduced J_c due to poor YBCO growth and a lower T_c. However, by optimizing the epitaxial growth of YBCO in the SZO nanocomposite, high quality films with promising pinning properties could be obtained. The BZO and the BHO nanocomposites exhibit excellent properties with the latter clearly showing the best-performance. The BHO nanocomposite shows a homogeneous distribution of the nanoparticles with an average diameter of 7 nm, which is among the smallest size ever achieved for artificial pinning centres in CSD. The small size of the final nanoparticles translates into a higher number of pinning centres compared to nanocomposites with more agglomerations. These nanoparticles and the high density of short Y124 intergrowths that they induce in the YBCO matrix lead to enhanced self-field J_c and a much smoother decay of J_c with magnetic field. F_p is also increased by a factor of 3.5 at 77 K while the J_c anisotropy is dramatically reduced by the addition of BHO nanocrystals, reaching some of the best superconducting properties ever achieved in low-fluorine CSD.

We conclude that CSD of low-fluorine colloidal YBCO solutions containing preformed double metal oxide nanocrystals is a reproducible method for high-quality films with enhanced pinning properties, which is ready to transfer to technical substrates for its use in coated conductor technology.

Supporting Information

Thermogravimetrical analysis of ligand; Scheme of Chemical Solution Deposition of colloidal YBCO inks; DLS analysis of BZO nanosuspension after storage for 3 months; X-Ray Diffractograms of nanocomposites between 5 and 140º; Extra Transmission Electron Microscopy images of pristine and nanocomposite films; Size distribution of nanoparticles in the YBCO matrix.

Acknowledgements

I.V.D and M.B. received funding for this work from the European Union's Horizon 2020 research and innovation programme under the Marie Skłodowska-Curie grant agreement No. H2020/2016-722071 (SynFoNY. www.synfony.eu). P.P. and H.H. received funding from the Jenny and Antti Wihuri Foundation.

The authors thank Dr. Katrien de Keukeleere, Dr. Maximiliam Hemgesberg, Armin Meyer and the rest of the SynFoNY team for their important contributions to this research project.

References

1. Larbalestier, D.; Gurevich, A.; Feldmann, D. M.; Polyanskii, A., High-Tc superconducting materials for electric power applications. In *Materials For Sustainable Energy*, World Scientific: **2011**; 311-320.
2. Baecker, M., Energy and superconductors–applications of high-temperature-superconductors. *Z. Kristallogr. Cryst. Mater.* **2011,** *226* (4), 343-351.
3. Obradors, X.; Puig, T., Coated conductors for power applications: materials challenges. *Supercond. Sci. Technol* **2014,** *27* (4), 044003.
4. Bäcker, M.; Baumann, A.; Brunkahl, O.; Erbe, M.; Schneller, T., Chemical Solution Deposition (CSD). *digital Ency. Appl. Phys* **2019**, 1-34.
5. Obradors, X.; Puig, T.; Pomar, A.; Sandiumenge, F.; Mestres, N.; Coll, M.; Cavallaro, A.; Roma, N.; Gazquez, J.; Gonzalez, J., Progress towards all-chemical superconducting $YBa_2Cu_3O_7$-coated conductors. *Supercond. Sci. Technol* **2006,** *19* (3), S13.
6. Feys, J.; Vermeir, P.; Lommens, P.; Hopkins, S. C.; Granados, X.; Glowacki, B. A.; Baecker, M.; Reich, E.; Ricard, S.; Holzapfel, B., Ink-jet printing of $YBa_2Cu_3O_7$ superconducting coatings and patterns from aqueous solutions. *J. Mater. Chem.* **2012,** *22* (9), 3717-3726.
7. Obradors, X.; Puig, T.; Ricart, S.; Coll, M.; Gazquez, J.; Palau, A.; Granados, X., Growth, nanostructure and vortex pinning in superconducting $YBa_2Cu_3O_7$ thin films based on trifluoroacetate solutions. *Supercond. Sci. Technol* **2012,** *25* (12), 123001.
8. MacManus-Driscoll, J.; Foltyn, S.; Jia, Q.; Wang, H.; Serquis, A.; Civale, L.; Maiorov, B.; Hawley, M.; Maley, M.; Peterson, D., Strongly enhanced current densities in superconducting coated conductors of $YBa_2Cu_3O_{7-x}$ + $BaZrO_3$. *Nat. Mater.* **2004,** *3* (7), 439.
9. Xu, A.; Delgado, L.; Khatri, N.; Liu, Y.; Selvamanickam, V.; Abraimov, D.; Jaroszynski, J.; Kametani, F.; Larbalestier, D., Strongly enhanced vortex pinning from 4 to 77 K in magnetic fields up to 31 T in 15 mol.% Zr-added (Gd, Y)-Ba-Cu-O superconducting tapes. *APL Mater.* **2014,** *2* (4), 046111.
10. Matsumoto, K.; Mele, P., Artificial pinning center technology to enhance vortex pinning in YBCO coated conductors. *Supercond. Sci. Technol* **2009,** *23* (1), 014001.

11. Erbe, M.; Hänisch, J.; Hühne, R.; Freudenberg, T.; Kirchner, A.; Molina-Luna, L.; Damm, C.; Van Tendeloo, G.; Kaskel, S.; Schultz, L., $BaHfO_3$ artificial pinning centres in TFA-MOD-derived YBCO and GdBCO thin films. *Supercond. Sci. Technol* **2015,** *28* (11), 114002.
12. Coll, M.; Guzman, R.; Garcés, P.; Gazquez, J.; Rouco, V.; Palau, A.; Ye, S.; Magen, C.; Suo, H.; Castro, H., Size-controlled spontaneously segregated Ba_2YTaO_6 nanoparticles in $YBa_2Cu_3O_7$ nanocomposites obtained by chemical solution deposition. *Supercond. Sci. Technol* **2014,** *27* (4), 044008.
13. Lei, L.; Zhao, G.; Xu, H.; Wu, N.; Chen, Y., Influences of Y_2O_3 nanoparticle additions on the microstructure and superconductivity of YBCO films derived from low-fluorine solution. *Mater. Chem. Phys.* **2011,** *127* (1-2), 91-94.
14. Gutierrez, J.; Llordes, A.; Gazquez, J.; Gibert, M.; Roma, N.; Ricart, S.; Pomar, A.; Sandiumenge, F.; Mestres, N.; Puig, T., Strong isotropic flux pinning in solution-derived $YBa_2Cu_3O_{7-x}$ nanocomposite superconductor films. *Nat. Mater.* **2007,** *6* (5), 367.
15. De Keukeleere, K.; Cayado, P.; Meledin, A.; Vallès, F.; De Roo, J.; Rijckaert, H.; Pollefeyt, G.; Bruneel, E.; Palau, A.; Coll, M., Superconducting $YBa_2Cu_3O_{7-\delta}$ nanocomposites using preformed ZrO_2 nanocrystals: growth mechanisms and vortex pinning properties. *Adv. Eng. Mater.* **2016,** *2* (10), 1600161.
16. Rijckaert, H.; Pollefeyt, G.; Sieger, M.; Hänisch, J.; Bennewitz, J.; De Keukeleere, K.; De Roo, J.; Hühne, R.; Bäcker, M.; Paturi, P., Optimizing nanocomposites through nanocrystal surface chemistry: superconducting $YBa_2Cu_3O_7$ thin films via low-fluorine metal organic deposition and preformed metal oxide nanocrystals. *Chem. Mater.* **2017,** *29* (14), 6104-6113.
17. Cayado, P.; De Keukeleere, K.; Garzón, A.; Perez-Mirabet, L.; Meledin, A.; De Roo, J.; Vallés, F.; Mundet, B.; Rijckaert, H.; Pollefeyt, G., Epitaxial $YBa_2Cu_3O_{7-x}$ nanocomposite thin films from colloidal solutions. *Supercond. Sci. Technol* **2015,** *28* (12), 124007.
18. Bretos, I.; Schneller, T.; Falter, M.; Bäcker, M.; Hollmann, E.; Wördenweber, R.; Molina-Luna, L.; Van Tendeloo, G.; Eibl, O., Solution-derived $YBa_2Cu_3O_{7-\delta}$ (YBCO) superconducting films with $BaZrO_3$ (BZO) nanodots based on reverse micelle stabilized nanoparticles. *J. Mater. Chem. C* **2015,** *3* (16), 3971-3979.
19. Martinez-Julian, F.; Ricart, S.; Pomar, A.; Coll, M.; Abellán, P.; Sandiumenge, F.; Casanove, M.-J.; Obradors, X.; Puig, T.; Pastoriza-Santos, I., Chemical Solution Approaches to $YBa_2Cu_3O_{7-d}$-Au Nanocomposite Superconducting Thin Films. *J. Nanosci. Nanotechnol.* **2011,** *11* (4), 3245-3255.
20. Rijckaert, H.; Cayado, P.; Nast, R.; Diez Sierra, J.; Erbe, M.; López Dominguez, P.; Hänisch, J.; De Buysser, K.; Holzapfel, B.; Van Driessche, I., Superconducting HfO_2-$YBa_2Cu_3O_{7-\delta}$ Nanocomposite Films Deposited Using Ink-Jet Printing of Colloidal Solutions. *Coatings* **2020,** *10* (1), 17.
21. Obradors, X.; Puig, T.; Li, Z.; Pop, C.; Mundet, B.; Chamorro, N.; Vallés, F.; Coll, M.; Ricart, S.; Vallejo, B., Epitaxial $YBa_2Cu_3O_{7-x}$ nanocomposite films and coated conductors from $BaMO_3$ (M= Zr, Hf) colloidal solutions. *Supercond. Sci. Technol* **2018,** *31* (4), 044001.
22. Li, Z.; Coll, M.; Mundet, B.; Chamorro, N.; Vallès, F.; Palau, A.; Gazquez, J.; Ricart, S.; Puig, T.; Obradors, X., Control of nanostructure and pinning properties in solution deposited $YBa_2Cu_3O_{7-x}$ nanocomposites with preformed perovskite nanoparticles. *Sci. Rep.* **2019,** *9* (1), 5828.
23. Llordes, A.; Zalamova, K.; Ricart, S.; Palau, A.; Pomar, A.; Puig, T.; Hardy, A.; Van Bael, M.; Obradors, X., Evolution of metal-trifluoroacetate precursors in the thermal decomposition toward high-performance $YBa_2Cu_3O_7$ superconducting films. *Chem. Mater.* **2010,** *22* (5), 1686-1694.
24. Palmer, X.; Pop, C.; Eloussifi, H.; Villarejo, B.; Roura, P.; Farjas, J.; Calleja, A.; Palau, A.; Obradors, X.; Puig, T., Solution design for low-fluorine trifluoroacetate route to $YBa_2Cu_3O_7$ films. *Supercond. Sci. Technol* **2015,** *29* (2), 024002.

25. Rijckaert, H.; De Roo, J.; Van Zele, M.; Banerjee, S.; Huhtinen, H.; Paturi, P.; Bennewitz, J.; Billinge, S.; Bäcker, M.; De Buysser, K., Pair Distribution Function Analysis of ZrO_2 Nanocrystals and Insights in the Formation of ZrO_2 - $YBa_2Cu_3O_7$ Nanocomposites. *Materials* **2018,** *11* (7), 1066.
26. De Roo, J.; Yazdani, N.; Drijvers, E.; Lauria, A.; Maes, J.; Owen, J. S.; Van Driessche, I.; Niederberger, M.; Wood, V.; Martins, J. C., Probing solvent–ligand interactions in colloidal nanocrystals by the NMR line broadening. *Chem. Mater.* **2018,** *30* (15), 5485-5492.
27. Rechberger, F.; Heiligtag, F. J.; Süess, M. J.; Niederberger, M., Assembly of $BaTiO_3$ nanocrystals into macroscopic aerogel monoliths with high surface area. *Angew. Chem.* **2014,** *53* (26), 6823-6826.
28. De Roo, J.; Van den Broeck, F.; De Keukeleere, K.; Martins, J. C.; Van Driessche, I.; Hens, Z., Unravelling the surface chemistry of metal oxide nanocrystals, the role of acids and bases. *J. Am. Chem. Soc.* **2014,** *136* (27), 9650-9657.
29. Rijckaert, H.; Hänisch, J.; Pollefeyt, G.; Bäcker, M.; Van Driessche, I., Influence of Ba^{2+} consumption and intermediate dwelling during processing of $YBa_2Cu_3O_7$ nanocomposite films. *J. Am. Ceram. Soc.* **2019,** *102* (7), 3870-3878.
30. Rikel, M.; Alekseeva, Z. M., Calculations and Experimental Methods in Evaluation of Phase Diagrams. Nauka: Moscow, **1985**; 160-164.
31. Scardi, P.; Leoni, M.; Delhez, R., Line broadening analysis using integral breadth methods: a critical review. *J. Appl. Crystallogr.* **2004,** *37* (3), 381-390.
32. Rikel, M.; Ehrenberg, J.; Mahachi, S.; Klein, M.; Hoppe, B.; Schutz, J.; Bock, J., Development of All-CSD Processes for Coated Conductors at Nexans: Limitations and Possible Solutions. *IEEE Trans. Appl. Supercond.* **2010,** *21* (3), 2928-2932.
33. Rikel, M. O.; Isfort, D.; Klein, M.; Ehrenberg, J.; Bock, J.; Specht, E. D.; Sun-Wagener, M.; Weber, O.; Sporn, D.; Engel, S., Simplified Procedure for Estimating Epitaxy of $La_2Zr_2O_7$-Buffered NiW RABITS Using XRD. *IEEE Trans. Appl. Supercond.* **2009,** *19* (3), 3307-3310.
34. Rikel, M.; Hellstrom, E., Development of 2201 intergrowths during melt processing Bi2212/Ag conductors. **2001,** *357*, 1081-1090.
35. Specht, E. D.; Goyal, A.; Li, J.; Martin, P. M.; Li, X.; Rupich, M., Stacking faults in $YBa_2Cu_3O_{7-x}$: Measurement using X-ray diffraction and effects on critical current. *Appl. Phys. Lett.* **2006,** *89* (16), 162510.
36. Talantsev, E.; Strickland, N.; Wimbush, S.; Storey, J.; Tallon, J.; Long, N., Hole doping dependence of critical current density in $YBa_2Cu_3O_{7-\delta}$ conductors. **2014,** *104* (24), 242601.
37. Talantsev, E.; Wimbush, S.; Strickland, N.; Xia, J.; D'Souza, P.; Storey, J.; Tallon, J.; Ingham, B.; Knibbe, R.; Long, N., Oxygen deficiency, stacking faults and calcium substitution in MOD YBCO coated conductors. **2012,** *23* (3), 7200205-7200205.
38. Koblichka-Veneva, A.; Sakai, N.; Tajima, S.; Murakami, M., YBCO. In *Handbook of superconducting materials*, Cardwell, D. A.; Ginley, D. S., Eds. CRC Press: **2003**; Vol. 1.
39. Qu, T.-M.; Lin, G.; Feng, F.; Deng, S.; Song, X., Biaxially textured (Bi, Pb)$_2Sr_2Ca_2Cu_3O_x$ thin films on $LaAlO_3$ substrates fabricated via chemical solution deposition method. *Supercond. Sci. Technol* **2019,** *32* (4), 045006.
40. Specht, E.; Sparks, C.; Dhere, A.; Brynestad, J.; Cavin, O.; Kroeger, D.; Oye, H., Effect of oxygen pressure on the orthorhombic-tetragonal transition in the high-temperature superconductor $YBa_2Cu_3O_x$. *Phys. Rev. B* **1988,** *37* (13), 7426-7434.
41. Llordés, A.; Palau, A.; Gázquez, J.; Coll, M.; Vlad, R.; Pomar, A.; Arbiol, J.; Guzmán, R.; Ye, S.; Rouco, V., *et al.*, Nanoscale strain-induced pair suppression as a vortex-pinning mechanism in high-temperature superconductors. *Nat. Mater.* **2012,** *11* (4), 329-336.
42. Palau, A.; Llordes, A.; Gibert, M.; Puig, T.; Pomar, A.; Obradors, X., Pinning landscape analysis in YBCO films with epitaxial and/or non-coherent BZO nanoparticles. *IEEE Trans. Appl. Supercond.* **2010,** *21* (3), 3243-3246.

43. Puig, T.; Gutiérrez, J.; Pomar, A.; Llordés, A.; Gázquez, J.; Ricart, S.; Sandiumenge, F.; Obradors, X., Vortex pinning in chemical solution nanostructured YBCO films. *Supercond. Sci. Technol* **2008,** *21* (3), 034008.
44. Guzman, R.; Gazquez, J.; Rouco, V.; Palau, A.; Magen, C.; Varela, M.; Arbiol, J.; Obradors, X.; Puig, T., Strain-driven broken twin boundary coherence in $YBa_2Cu_3O_{7-\delta}$ nanocomposite thin films. *Appl. Phys. Lett* **2013,** *102* (8), 081906.
45. Obradors, X.; Puig, T.; Gibert, M.; Queralto, A.; Zabaleta, J.; Mestres, N., Chemical solution route to self-assembled epitaxial oxide nanostructures. *Chem. Soc. Rev.* **2014,** *43* (7), 2200-2225.
46. Pinol, S.; Sandiumenge, F.; Martinez, B.; Gomis, V.; Fontcuberta, J.; Obradors, X.; Snoeck, E.; Roucau, C., Enhanced critical currents by CeO_2 additions in directionally solidified $YBa_2Cu_3O_7$. *Appl. Phys. Lett.* **1994,** *65* (11), 1448-1450.
47. Diez Sierra, J.; Rikel, M.; Rijckaert, H.; Falter, M.; Khan, M.; Huhtinen, H.; Paturi, P.; Bäcker, M.; Van Driessche, I. In *Oxygen doping effects in CSD-YBCO nanocomposite films with preformed nanocrystals*, EUCAS 2019, 2019.
48. Cantoni, C.; Gao, Y.; Wee, S. H.; Specht, E. D.; Gazquez, J.; Meng, J.; Pennycook, S. J.; Goyal, A., Strain-driven oxygen deficiency in self-assembled, nanostructured, composite oxide films. *ACS Nano* **2011,** *5* (6), 4783-4789.
49. Wee, S. H.; Zuev, Y. L.; Cantoni, C.; Goyal, A., Engineering nanocolumnar defect configurations for optimized vortex pinning in high temperature superconducting nanocomposite wires. *Sci. Rep.* **2013,** *3*, 2310.
50. Angrisani Armenio, A.; Pinto, V.; Mancini, A.; Augieri, A.; Galluzzi, V.; Rizzo, F.; Rufoloni, A.; Vannozzi, A.; Celentano, G., Analysis of the Growth Process and Pinning Mechanism of Low-Fluorine MOD $YBa_2Cu_3O_{7-d}$ Films With and Without $BaZrO_3$ Artificial Pinning Centers. **2015,** *25*.
51. Petrisor, T.; Mos, R.; Nasui, M.; Gabor, M.; Augieri, A.; Celentano, G.; De Felicis, D.; Bemporad, E.; Ciontea, L., The Vortex Path Model Analysis of the Field Angle Dependence of the Critical Current Density in Nanocomposite $YBa_2Cu_3O_{7-x}$–$BaZrO_3$ Films Obtained by Low Fluorine Chemical Solution Deposition. **2014,** *27* (11), 2493-2500.
52. Civale, L.; Maiorov, B.; MacManus-Driscoll, J.; Wang, H.; Holesinger, T.; Foltyn, S.; Serquis, A.; Arendt, P., Identification of intrinsic ab-plane pinning in $YBa_2Cu_3O_7$ thin films and coated conductors. *IEEE Trans. Appl. Supercond.* **2005,** *15* (2), 2808-2811.
53. Diaz, A.; Mechin, L.; Berghuis, P.; Evetts, J., Evidence for vortex pinning by dislocations in $YBa_2Cu_3O_{7-\delta}$ low-angle grain boundaries. *Phys. Rev. Lett.* **1998,** *80* (17), 3855.
54. Nelson, D. R.; Vinokur, V., Boson localization and correlated pinning of superconducting vortex arrays. *Phys. Rev. B* **1993,** *48* (17), 13060.
55. Tachiki, M.; Takahashi, S., Strong vortex pinning intrinsic in high-Tc oxide superconductors. *Solid State Commun.* **1989,** *70* (3), 291-295.
56. Maiorov, B.; Baily, S.; Zhou, H.; Ugurlu, O.; Kennison, J.; Dowden, P.; Holesinger, T.; Foltyn, S.; Civale, L., Synergetic combination of different types of defect to optimize pinning landscape using $BaZrO_3$-doped $YBa_2Cu_3O_7$. *Nat. Mater.* **2009,** *8* (5), 398.
57. Paturi, P.; Irjala, M.; Huhtinen, H., Greatly decreased critical current density anisotropy in $YBa_2Cu_3O_{6+x}$ thin films ablated from nanocrystalline and $BaZrO_3$-doped nanocrystalline targets. *J. Appl. Phys.* **2008,** *103* (12), 123907.
58. Malmivirta, M.; Yao, L.; Huhtinen, H.; Palonen, H.; van Dijken, S.; Paturi, P., Three ranges of the angular dependence of critical current of $BaZrO_3$ doped $YBa_2Cu_3O_{7-\delta}$ thin films grown at different temperatures. *Thin Solid Films* **2014,** *562*, 554-560.
59. Aye, M. M.; Khan, M. Z.; Rivasto, E.; Tikkanen, J.; Huhtinen, H.; Paturi, P., Role of columnar defect size in angular dependent flux pinning properties of YBCO thin films. *IEEE Trans. Appl. Supercond.* **2019,** *29* (5), 1-5.

60. Paturi, P., The vortex path model and angular dependence of J_c in thin YBCO films deposited from undoped and $BaZrO_3$-doped targets. *Supercond. Sci. Technol* **2010,** *23* (2), 025030.
61. Long, N., Model for the angular dependence of critical currents in technical superconductors. *Supercond. Sci. Technol* **2008,** *21* (2), 025007.
62. Long, N.; Strickland, N.; Talantsev, E., Modeling of vortex paths in HTS. *IEEE Trans. Appl. Supercond.* **2007,** *17* (2), 3684-3687.
63. Tarantini, C.; Iida, K.; Hänisch, J.; Kurth, F.; Jaroszynski, J.; Sumiya, N.; Chihara, M.; Hatano, T.; Ikuta, H.; Schmidt, S., Intrinsic and extrinsic pinning in NdFeAs (O, F): vortex trapping and lock-in by the layered structure. *Sci. Rep.* **2016,** *6*, 36047.
64. Oussena, M.; De Groot, P.; Porter, S.; Gagnon, R.; Taillefer, L., Vortex channeling along twin planes in $YBa_2Cu_3O_{7-x}$. *Phys. Rev. B* **1995,** *51* (2), 1389.
65. Palau, A.; Durrell, J.; MacManus-Driscoll, J.; Harrington, S.; Puig, T.; Sandiumenge, F.; Obradors, X.; Blamire, M., Crossover between channeling and pinning at twin boundaries in $YBa_2Cu_3O_7$ thin films. *Phys. Rev. Lett.* **2006,** *97* (25), 257002.
66. Rouco, V.; Palau, A.; Guzman, R.; Gazquez, J.; Coll, M.; Obradors, X.; Puig, T., Role of twin boundaries on vortex pinning of CSD YBCO nanocomposites. *Supercond. Sci. Technol* **2014,** *27* (12), 125009.
67. Yamasaki, H., Origin of collapse of $J_c(\theta)$ peaks at H//c in low temperatures in (RE) BCO thin films with nanorods. *Supercond. Sci. Technol* **2019,** *32* (9), 09LT01.
68. Palonen, H.; Huhtinen, H.; Paturi, P., Growth Condition Dependence of Microcracks in YBCO Thin Films Pulsed Laser Deposited on $NdGaO_3$ (001) Substrates. *IEEE Trans. Appl. Supercond.* **2014,** *25* (3), 1-4.
69. Khan, M.; Zhao, Y.; Wu, X.; Malmivirta, M.; Huhtinen, H.; Paturi, P., Improved interface growth and enhanced flux pinning in YBCO films deposited on an advanced IBAD-MgO based template. *Physica C* **2018,** *545*, 50-57.